Engineering Failure Analysis 172 (2025) 109403

Contents lists available at ScienceDirect

Engineering Failure Analysis

journal homepage: www.elsevier.com/locate/engfailanal

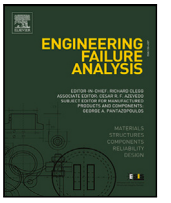

Fatigue of Ti6Al4V manufactured by PBF-LB: A comparison of failure mechanisms between net-shape and electro-chemically milled surface conditions

Tatiana Risposi [a,1], Lorenzo Rusnati [a,1], Luca Patriarca [a], Alex Hardaker [c], Dawid Luczyniec [d], Stefano Beretta [a,b,*]

[a] Politecnico di Milano, Department of Mechanical Engineering, via La Masa 1, 20156 Milano, Italy
[b] Auburn University, National Center for Additive Manufacturing Excellence (NCAME), Auburn, AL 36849, USA
[c] MTC–National Centre for AM, Coventry CV7 9JU, UK
[d] European Space Agency ESTEC, Keplerlaan 1, 2200 AG Noordwijk-ZH, The Netherlands

ARTICLE INFO

Keywords:
Laser-powder bed fusion
Net-shape
Hirtisation
Fatigue
Contouring defects

ABSTRACT

In the recent years, metal additive manufacturing (AM) has acquired large interest for many industrial applications, principally due to the capability to produce parts with complex geometry. The critical aspect of AM parts is the sensitivity to surface anomalies due to net-shape surfaces, i.e surface microcracks and protrusions, localized stresses caused by coarse surface roughness, or sub-surface features placed below the outer skin in the contour region. To reduce the surface roughness and increase the fatigue properties, proper post-process treatments can be applied. This work investigates the improvement in surface quality and fatigue properties due to the electro-chemical milling process of Hirtisation® compared with net-shape condition, on samples manufactured in Ti6Al4V by laser-powder bed fusion (PBF-LB). Post-processing led to a reduction of surface roughness due to the removal of the peaks and sharp valleys that act as crack initiation sites during fatigue tests, but it exposed the sub-skin contouring defects to the free surface. These were the crack initiation sites resulting in a limited improvement of the potential benefits produced by Hirtisation®. This was confirmed by fatigue life predictions based on propagation of surface features and contouring anomalies.

1. Introduction

Additive manufacturing (AM) offers several significant advantages, including the ability to produce parts with complex geometries with minimal post-processing, reduced material waste, and the flexibility to work with both metals and plastics [1]. This study focuses on the laser-powder bed fusion (PBF-LB) process, specifically using the Ti6Al4V alloy, which is widely utilized in various industries such as aerospace [2,3], chemical, marine, automotive, and medical sectors [4–6]. The large applicability of Ti6Al4V is attributed to its high corrosion resistance, excellent bio-compatibility, high strength, and a good balance of mechanical properties relative to its density, in addition to its high weldability.

Although recent literature has demonstrated that the static properties of Ti6Al4V alloy produced by PBF-LB process are comparable to those of wrought titanium alloys [7–11], the fatigue performances are generally reduced because the PBF-LB process

* Corresponding author at: Politecnico di Milano, Department of Mechanical Engineering, via La Masa 1, 20156 Milano, Italy.
E-mail address: stefano.beretta@polimi.it (S. Beretta).

[1] These authors share the first authorship as they have contributed equally to this work.

https://doi.org/10.1016/j.engfailanal.2025.109403
Received 5 December 2024; Received in revised form 6 February 2025; Accepted 7 February 2025
Available online 14 February 2025

Nomenclature

Acronyms

AM	Additive manufacturing
CPCA	Compression pre-cracking constant amplitude
CPLR	Compression pre-cracking load reduction
EBSD	Electron back-scatter diffraction
EDM	Electrical discharge machining
EVS	Extreme values statistics
FCG	Fatigue crack growth
IPF	Inverse pole figure
LEVD	Largest extreme values distribution
OPS	Oxide polishing suspension
PBF-EB	Electron beam powder bed fusion
PBF-LB	Laser-powder bed fusion
SEB	Single edge-notched bending
SEM	Scanning electron microscope

Symbols

δ	Scale parameter of the LEVD
$\Delta K_{th,LC}$	Long crack threshold stress intensity factor range
ΔK_{th}	Threshold stress intensity factor range
$\Delta\sigma_{w,0}$	Fatigue limit stress range in absence of defects
$\Delta\sigma_{w}$	Fatigue limit stress range
ε_f	Elongation at fracture
λ	Position parameter of the LEVD
λ_c	Cut-off wavelength
σ	Stress
$\sigma_{\log N}$	Standard deviation of the logarithmic life
σ_w	Fatigue limit stress amplitude
$\sqrt{\text{area}}$	Murakami's defect size
$\sqrt{\text{area}}_{50\%}$	Average defect size
$\sqrt{\text{area}}_0$	El-Haddad parameter
A	Fit parameter of the S–N curve
a	Crack depth
B	Slope of the S–N curve
C	Fit parameter of the NASGRO equation
c	Crack width
E	Young's modulus
f	Newman's crack opening function
F_{LEVD}	Cumulative density function of the LEVD
K_{Ic}	Fracture toughness
m	Fit parameter of the NASGRO equation
N	Fatigue cycles
N_{lim}	Fatigue cycles at the knee point
p	Fit parameter of the NASGRO equation
q	Fit parameter of the NASGRO equation
R	Load ratio
S_a	Aerial arithmetic roughness
S_p	Maximum peak height
$S_{p,m}$	Mean profile peak height
S_q	Quadratic mean of profile height
S_v	Maximum valley depth

S_z	Maximum peak to valley height
t_{max}	Maximum crack depth
UTS	Ultimate tensile strength
Y	Shape factor
YS	Yield strength

Table 1
Chemical analysis of Ti6Al4V powder, expressed as Wt.%.

Al	V	Ti	O	N	H	Fe	C	Y	Others
6.29	4.04	bal.	0.09	0.01	0.001	0.04	0.01	<0.001	<0.40

produces inherently rough surfaces from which cracks can nucleate [12–14]. On PBF-LB surfaces, features like ridges and troughs with steep walls can be distinguished [15,16]. These surface features are particularly detrimental for structural components as they create high stress concentration areas [17–19]. Additionally, sub-surface defects, such as pores and lack of fusion, can also contribute to crack nucleation [14,20–22]. The occurrence of these defects depends on process parameters like laser power, scanning speed, hatch spacing, and layer thickness [19,23,24]. Another important factor affecting the presence of surface and sub-surface defects is the scanning strategy. Typically, contour scanning strategies are used to improve surface quality [25–27], although multiple defects often appear in the sub-surface, contour region [28]. The location of these defects depends on the contour depth and parameters, and they can have sharper shapes than defects found in the hatch [29].

Recent studies have shown that the fatigue properties of net-shape PBF-LB materials can be enhanced through appropriate post-processing treatments that reduce surface roughness. This is particularly important because fatigue cracks often initiate at multiple locations on the surface's valleys [18,30–32]. One method for reducing surface roughness is chemical milling, a process that removes layers of material using liquid chemical compounds. By utilizing chemical-based surface treatments, there are no geometric constraints on the areas that can be treated, making them particularly effective for hard-to-access locations that are challenging for traditional machining tools [31,33]. As a result, chemical treatments have received special attention, and their effects on AM parts were explored in several studies [34,35]. However, certain structures, such as strut-based lattices, exhibit limitations in chemical etching techniques due to restricted fluid flow, leaving unmelted particles trapped deep within. These particles act as stress concentration points and are detrimental for the fatigue performances of the manufactured parts [36]. To overcome some of the limitations of the traditional chemical etching techniques, a new chemically-based post-process treatment, called Hirtisation®, was developed and it is currently supplied by RENA Technologies GmbH (Austria). Hirtisation® is a process that combines electro-chemical pulse methods, flow and particle-assisted chemical removal, and chemical surface treatment, thereby integrating the advantages from each process route. Published works have investigated the effect of Hirtisation® on AlSi10Mg samples manufactured by the PBF-LB process [31,37,38], as well as on Ti6Al4V manufactured by the electron beam powder bed fusion (PBF-EB) process [29,39–41]. However, to the authors' knowledge, there is limited information available regarding the effect of the Hirtisation® process on the fatigue properties of AMed materials, particularly Ti6Al4V, which is one of the most widely used materials in aerospace applications.

This study examines the surface quality of net-shape Ti6Al4V produced by the PBF-LB process before and after undergoing the Hirtisation® post-process. In particular, it focuses on the impact of residual porosities and surface roughness on fatigue performances. A comprehensive testing campaign was designed to evaluate the fatigue and fracture properties of Ti6Al4V manufactured by the PBF-LB process, comparing fatigue specimens differing by their surface condition.

2. Materials and experiments

2.1. Specimens manufacturing

The test campaign presented in this study involved tests conducted on specimens oriented with the load direction parallel to the building direction. The specimens' geometries are reported in Fig. 1.

All the Ti6Al4V specimens were manufactured by the research organization Manufacturing Technology Centre (MTC, Coventry, UK) on a Renishaw 500Q PBF-LB machine equipped with 4 × 500 W Prism Ytterbium fibre pulsed lasers with dynamic focusing. The oxygen content was controlled and measured by sensors in the Renishaw AM500Q, a maximum O_2 limit of 1000 ppm is set on the machine, however the build process is performed in a lower O_2 atmosphere, with a measured content around 100 ppm through the build. Powder composition is reported in Table 1. Particle size distribution was estimated through laser size diffraction and showed a median dimension equal to 31.2 μm, with the 10% and 90% percentiles equal to 21.4 μm and 45.1 μm respectively. The scan strategy used two contour scans, offset from each other by 50 μm and with the outer contour offset from the nominal part geometry by 100 μm, Fig. 1(c). The contour was completed before the bulk hatching in a spot melting mode, which translates to very rapid exposure of beam as an array of individual spots.

Table 2
Build parameters for Ti6Al4V specimens.

Region	Parameter	Value
	Layer thickness [μm]	60
Bulk	Scan strategy	Stripe
	Power [W]	180
	Point distance [μm]	65
	Exposure time [μs]	110
	Hatch distance [μm]	95
Contour	Contour offset [μm]	50
	Power [W]	320
	Point distance [μm]	30
	Exposure time [μs]	20
	Hatch distance [μm]	60

Table 3
Tensile properties of PBF-LB/Ti6Al4V alloy in net-shape condition.

UTS [MPa]	YS [MPa]	E [MPa]	ε_f[%]
1187	1146	114,469	12

The build was conducted in an inert build chamber evacuated and filled with Argon shielding gas. During manufacturing, the build plate was maintained at 170 °C. A summary of the MTC's standard process parameters is reported in Table 2. The specimens were then stress-relieved through a heat treatment consisting of heating to 650 °C at atmospheric pressure in Argon for a soaking time of 2 h. This was followed by a controlled cooling phase inside the furnace, completed in less than 5 h.

The cylindrical specimens for axial fatigue (Fig. 1(a)) were characterized by a diameter of the cross section of 6 mm, in compliance with ASTM E466 [42]. The specimens were successively machined in the grip region, while the cross-section was left in the net-shape condition.

Tensile properties were evaluated on two net-shape specimens tested under a MTS RT100 system with a load capacity of 100 kN. The results are listed in Table 3.

The single edge-notched bending (SEB) specimens (Fig. 1(b)) were manufactured with the crack plane parallel to the building plate. The external surfaces were milled to guarantee the tolerances required. The notches were obtained by means of electrical discharge machining (EDM) which guaranteed a notch tip with a radius of 150 μm, free of alpha case formation.

2.2. Hirtisation®

The fatigue specimens were split into two groups: net-shape condition and treated with Hirtisation®. Hirtisation® was conducted by RENA Technologies GmbH. The treatment comprises two consecutive steps: (i) softening of support structures and powder adhesions in Ti-Auxilex electrolyte, (ii) detachment of softened support structure, detachment of powder adhesions and polishing in Ti-Delevatex electrolyte. Between each treatment step, the parts were rinsed in a de-ionized water basin and were dried in a vacuum drying unit. Prior to the manufacturing of the specimens, different trials were conducted on coupons to tune the electro-chemical milling parameters to achieve a removal up to 200 μm from the treated surface. Nonetheless, the post-process, once applied to the fatigue specimens, removed material for an average of 66 μm in radial direction. This limited material removal is the cause of the peculiar failure mechanism described in the following sections.

2.3. Microstructure

The near surface microstructure was evaluated on cross sections taken from the gauge length of two axial specimens, one in net-shape condition and one treated with Hirtisation®. The samples were cut in a direction parallel to the load axis, were mounted into an epoxy resin and polished starting with sand-paper with granularity of 220, followed by a 9 μm diamond paper and concluding with a Colloidal Silica oxide polishing suspension (OPS). An electron back-scatter diffraction (EBSD) analysis was performed by scanning electron microscopy (SEM) in order to investigate the microstructure.

Porosity measurements were conducted on witness samples printed with the specimens. Four samples were located in the corners of each build. The witness specimens were prepared by cutting along the vertical plate and polishing the samples to enable analysis over the full height of the cubes. Image fractions were then taken from the images of the sample sections to give an indication of porosity levels in the builds, in accordance with ASTM F3637 standard [43]. Porosity levels measured on the witness coupons portrayed a stable density across the builds. The average relative density was 99.97% with a standard deviation of 0.02%; the maximum density was recorded at 99.99%, whereas the minimum value was 99.89%.

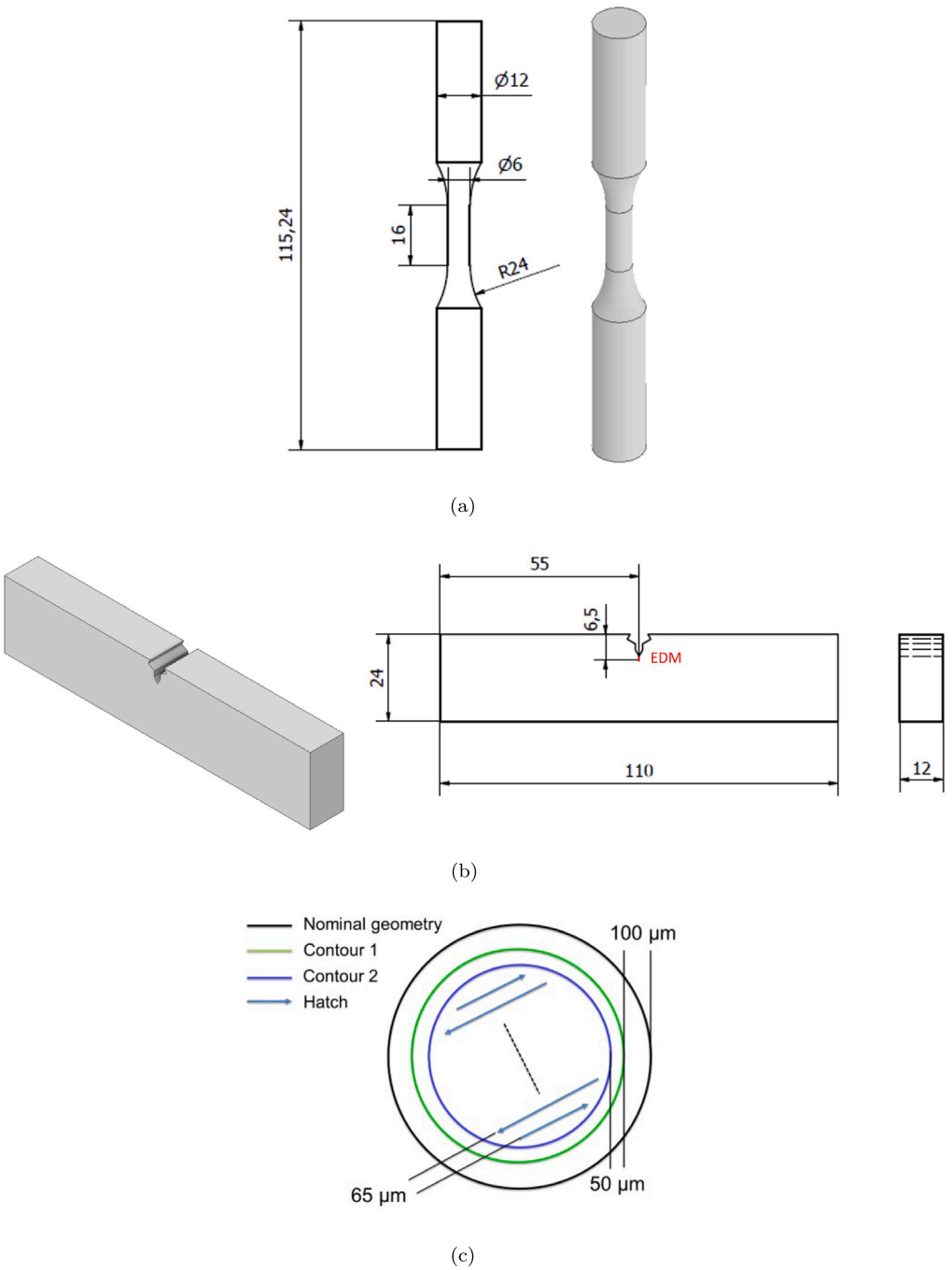

Fig. 1. (a) Axial specimen for high cycle fatigue tests; (b) Single edge-notched bending specimen for fatigue crack growth tests; (c) Printing strategy represented on the cross section of the axial specimens.

2.4. Roughness measurement

Roughness measurements on net-shape surface and on surface after Hirtisation® were performed with *Alicona InfiniteFocus* FV (Focus-Variation). One specimen for each surface condition was analysed. The measurements were done along the cylinders' axial direction, on 4 areas of 1 mm × 15 mm each; each region was distanced by a 90 degrees rotation. These acquisitions were carried out at a vertical resolution of 60 µm and lateral resolution of 2 µm. The primary profiles extracted from Alicona were filtered with a Robust Gaussian filter with a cut-off wavelength $\lambda_c = 3$ mm.

2.5. Fatigue tests

The fatigue tests were performed at a stress ratio R = −1, in air, at room temperature, on the MTS 810 servo-hydraulic machine with a load capacity of 100 kN. The run-out condition was set at 10^7 cycles, although a single test was marked as run-out at 5×10^6 cycles. The testing frequency was chosen within the range of 20 ÷ 40 Hz to balance the accuracy of the load control by the servo-hydraulic equipment and the testing time. The load level was calculated for each specimen, based on the average diameter measured on 3 sections at different heights along the gauge length. All fracture surfaces were analysed by SEM, using the Zeiss EVO50 system, to identify the killer defect at the origin of the fatigue failure.

2.6. Fatigue crack growth tests

SEB specimens were initially pre-cracked under the MTS 810 servo-hydraulic system with load capacity of 100 kN. The selected pre-cracking procedure consisted in the application of compressive cyclic loadings with the aim of nucleating an initial closure-free crack at the EDM notch [44]. In particular, the first compressive load cycle generates yielding in the region of the notch, thus leading to residual tensile stresses that, subjected to the subsequent load cycles, nucleate a crack. Successively, the residual stresses decrease with the crack advancement until the crack driving force is below the threshold and the crack arrests [45]. Specimens were loaded in fatigue with a maximum compressive load of 40 kN for 2×10^6 cycles to develop an average pre-crack size of 47 μm.

After pre-cracking, crack growth rate tests were conducted for four load ratios: R = 0.7, R = 0, R = −1 and R = −2. Two types of tests were performed: (i) determination of the Paris region via Compression Pre-cracking-Constant Amplitude (CPCA) procedure, (ii) measure of the crack growth threshold, $\Delta K_{th,LC}$, via Compression Pre-cracking-Load Reduction method (CPLR). During the tests, a clip-on-gauge was utilized to monitor the crack length through the compliance method. At the end of the fatigue crack growth tests, the specimens were statically broken and the fracture surfaces were investigated by means of a stereo microscope; the real final crack lengths were measured and the acquired experimental data were corrected accordingly.

3. Results

3.1. Micrographs of surfaces and microstructural characterization

Micrographs of polished longitudinal sections near the sample surfaces were examined using SEM, both in net-shape condition and after Hirtisation®, as shown in Fig. 2. The difference in surface texture between the two conditions is clearly visible, with the post-Hirtisation® surface appearing smoother and more weavy. In contrast, the net-shape surface exhibits deep and sharp valleys that act as crack initiation sites during fatigue tests. Sub-surface features in the contour region can also be observed for both surface conditions, as indicated by the yellow dashed circles in Fig. 2.

The use of Hirtisation® led to an average reduction of the diameter of the specimens' gauge region of 132 μm. The removal exceeded the ten-point height parameter S_{10z} of the surface roughness evaluated on the net-shape specimens (additional details are reported in Section 3.2). As a result, all surface features from the net-shape surfaces were removed. However, this material removal brought sub-surface contouring anomalies closer to the surface. For example, Fig. 2 shows a sub-surface defect located at a depth of 52 μm in a surface-treated specimen, compared to 139 μm in the net-shape condition. These defects, being closer to the surface, may become critical and act as killer defects.

Fig. 2 also presents inverse pole figure (IPF)-z maps of the regions surrounding the sub-surface pores. Consistent with previous studies [8,46,47], the microstructure of Ti6Al4V shows very fine α' martensite with columnar β grains, aligned opposite to the cooling direction due to the high cooling rate of the PBF-LB process. This microstructure is responsible for the high strength and low ductility of laser-based AM Ti6Al4V alloy [48]. In both conditions, the microstructures near the surface are very similar, with no observable microstructural alterations after the Hirtisation® post-process.

3.2. Roughness measurement

The topography of the surfaces of the fatigue specimens' measured surfaces is presented in Fig. 3, alongside detailed SEM images of the surfaces in the two conditions. As expected, the net-shape specimens exhibit higher surface roughness and a significant presence of partially molten particles, see Fig. 3(a). Roughness data from net-shape fatigue specimens are in line with the expectations as the values are comparable with legacy data by The MTC, acquired on previous prints on Renishaw AM500Q, showing an arithmetic roughness R_a = 11.94 μm. After Hirtisation®, the high peaks are generally removed. However, as shown in Fig. 3(b), slight waviness and ridges with scattered craters in between can still be observed in accordance with [31].

Areal surface roughness values for the two surface conditions, by averaging four measurements performed on each sample, are listed in Table 4, along with the percentage reduction in roughness parameters after Hirtisation®. The roughness profiles obtained by the four areal measurements performed on one specimen for each surface condition are reported in Fig. 4(a) for net-shape condition, and Fig. 4(b) after Hirtisation®. The graphs evidence that the post-process changed the surface texture, since all the roughness parameters are decreased in value. The maximum peak height, S_p, is the parameter most affected by Hirtisation® post-process with a reduction of 57%. This is also visible from the height maps of the surfaces before and after the post-process, reported in Fig. 3.

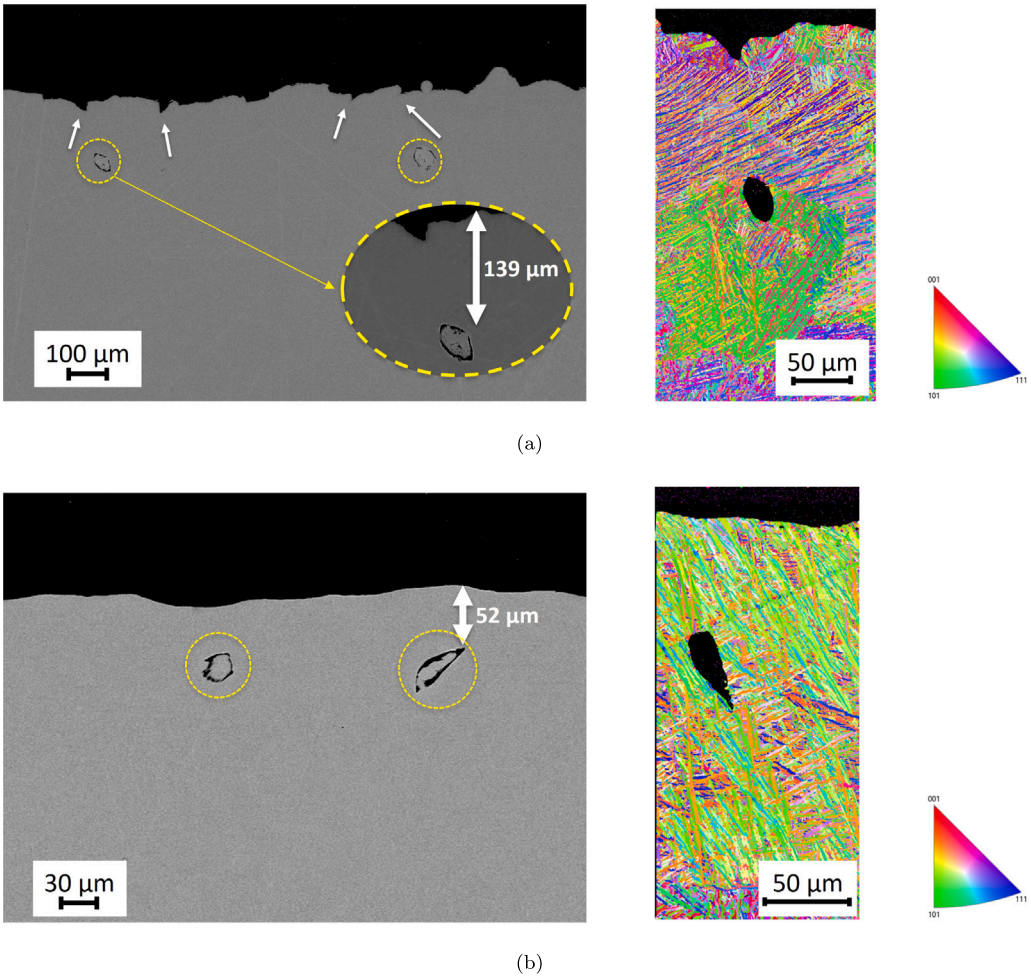

Fig. 2. Micrographs of the sample surfaces and related IPF-z maps: (a) net-shape condition shows sharp valleys indicated with white arrows and sub-surface defects highlighted in yellow, (b) surface after Hirtisation® post-processor shows a waviness surface with sub-surface defects closer to the surface.

Table 4
Areal roughness parameters from Alicona acquisitions, for Ti6Al4V specimens in two surface conditions.

Surface condition	S_a [µm]	S_q [µm]	S_p [µm]	S_v [µm]	S_z [µm]
Net-shape	11.6	15.0	88.9	73.0	162.0
Hirtisation®	6.8	9.0	37.9	49.1	87.0
Reduction	41%	40%	57%	32%	46%

3.3. Fatigue tests

The fatigue results are presented as S–N diagrams for both net-shape and after Hirtisation® conditions in Fig. 5. The regression line, representing 50% failure probability, was obtained by fitting the experimental data in the finite region with Eq. (1), in accordance with ASTM E739 [49]:

$$N = A\sigma^B \tag{1}$$

The fitting parameters, determined using the maximum likelihood method, are listed in Table 5. Scatter in the data was accounted for by fitting the experimental data with a log-normal distribution, assuming a constant standard deviation σ_{logN}. Table 5 also reports the experimental fatigue limit range, $\Delta\sigma_w$, and the number of cycles to failure N_{lim} at the knee-point of the S–N curves. The fatigue limits were calculated applying the Dixon up and down method [50].

A comparison between the S–N curves for net-shape condition and after Hirtisation® is presented in Fig. 5, in which the experimental points, the log-normal fits and the 95% scatter bands are reported. It is possible to observe how the specimen subjected to Hirtisation® have enhanced fatigue performance compared to the net-shape condition. In the finite life region, fatigue life is

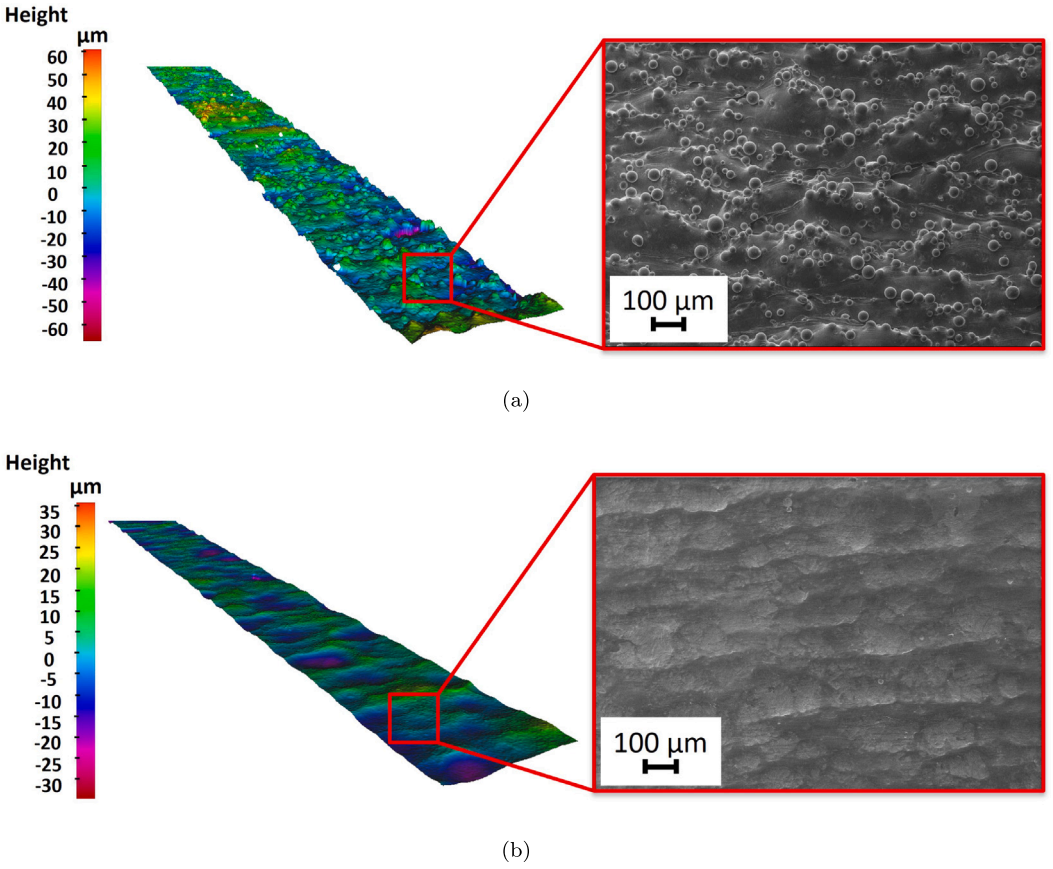

Fig. 3. Elaboration of the surfaces acquired by focus variation microscopy and SEM images of cylindrical specimens' surfaces: (a) net-shape surface, (b) surface after Hirtisation®.

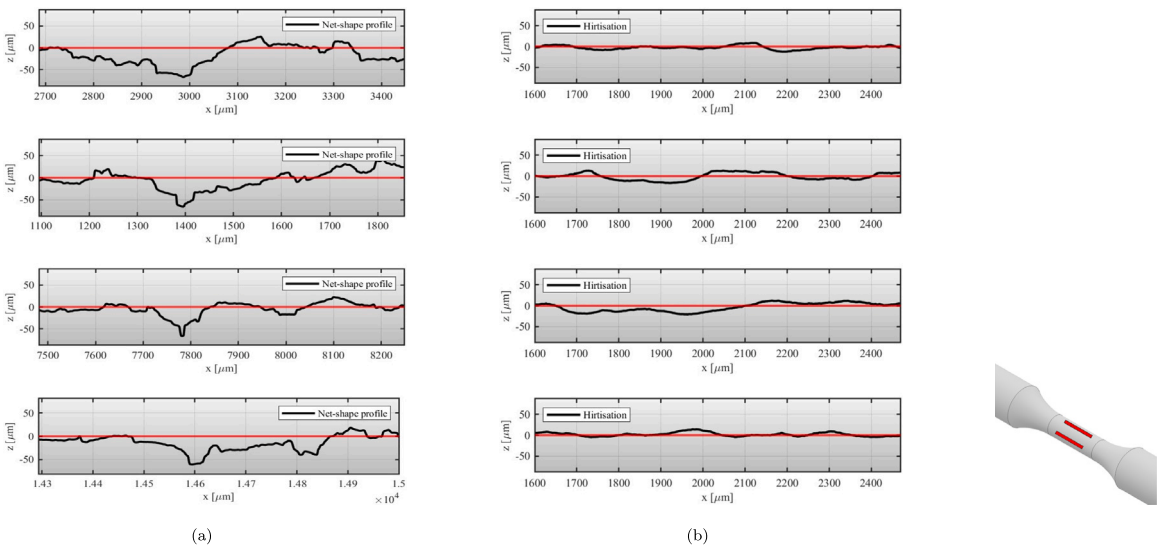

Fig. 4. Roughness profiles extracted from the areal measurements: (a) surface in net-shape condition, (b) surface after Hirtisation®.

Table 5
Parameters of the S–N curves for the two series of Ti6Al4V specimens.

Surface condition	σ_{logN}	$log_{10}(A)$	B	N_{lim} [cycles]	$\Delta\sigma_w$ [MPa]
Net-shape	0.1394	5.1384	−4.53	629,265	420
Post-Hirtisation®	0.1043	5.1672	−4.71	580,369	480

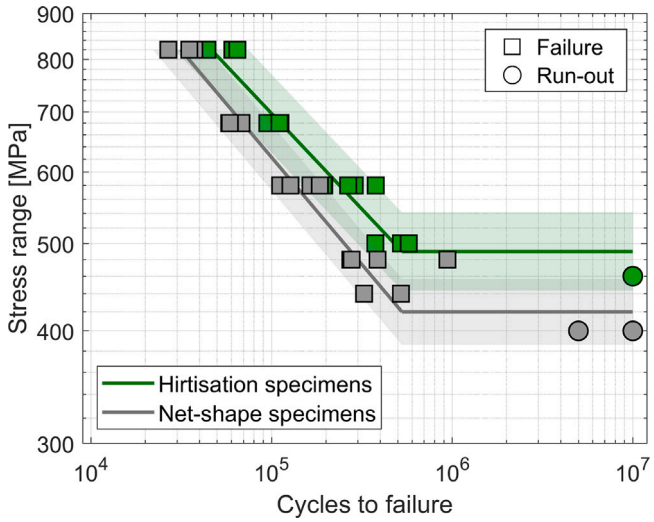

Fig. 5. S–N curves of Ti6Al4V alloy from fatigue tests conducted at R = −1.

significantly increased by a factor ≈1.6, with the S–N diagrams having a similar slope. However, the increase of the fatigue limit is less pronounced: the Hirtisation® process resulted in a fatigue limit of $\Delta\sigma_w$ = 480 MPa, compared to $\Delta\sigma_w$ = 420 MPa for the net-shape condition.

It is important to note that removing the surface layer has two primary effects, particularly effective in the fatigue limit region. First, it reduces surface roughness, which positively impacts fatigue life. Simultaneously, the Hirtisation® process reduces the average distance between sub-surface defects and the surface, increasing the criticality of these defects. This second effect partially offsets the positive impact of surface roughness reduction. A detailed discussion of the different types of killer defects identified through fracture surface analysis is provided in Section 4.

3.4. Fatigue crack growth tests

The results of the experimental crack growth tests are presented in Fig. 6(a) for the four load ratios investigated in the present study (i.e. R = 0.7, 0, −1 and −2), while Fig. 6(b) presents the experimental $\Delta K_{th,LC}$ as a function of the load ratio R. These quantities are also reported in Table 6. The procedure adopted to fit the $\Delta K_{th,LC}$ values, the solid red line in Fig. 6(a), is the same followed by Beretta et al. [51] and by Barricelli et al. [52]. The crack growth properties of the present Ti6Al4V alloy are coherent with values from Polimi database on the same material, the same printing direction and with heat treatments at temperature that guarantee a similar microstructure [52,53], as well as with literature data [54,55].

The solid lines in Fig. 6(a) represent the fitting of experimental crack growth data with the NASGRO equation [56]:

$$\frac{da}{dN} = C\left[\left(\frac{1-f}{1-R}\right)\Delta K\right]^m \frac{(1-\frac{\Delta K_{th}}{\Delta K})^p}{(1-\frac{K_{max}}{K_c})^q} \tag{2}$$

in which the fitting parameters C, m and p were determined according to the available experimental data, while q was set equal to zero since it describes the zone of the Paris region in which there is unstable crack propagation ($K_{max} \longrightarrow K_c$) which was not covered by the experimental tests. Similar results in the Paris region were obtained by Cain et al. [57].

4. Analysis of critical defects

4.1. Measurement of surface features

The fracture mechanics approach proposed by Murakami [58] was adopted for the analysis of the fatigue limit's dependence on defect size. The fracture surfaces of fatigue samples were analysed by means of a SEM, revealing two crack initiation features:

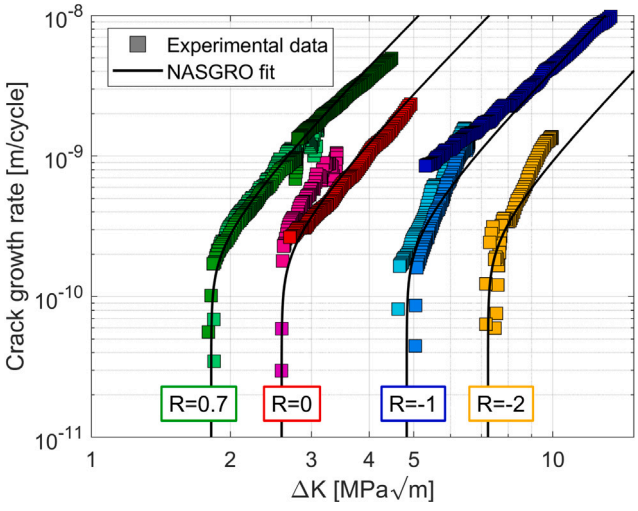

(a)

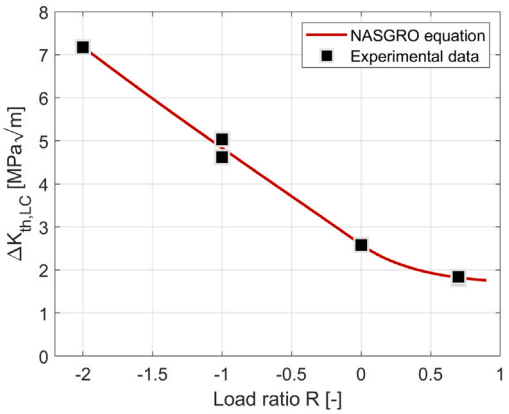

(b)

Fig. 6. Fatigue crack growth tests on Ti6Al4V alloy: (a) NASGRO fit obtained from experimental crack growth data, (b) $\Delta K_{th,LC}$ versus load ratio R variation as experimental data and description by the NASGRO model.

Table 6
Experimentally determined and results of the NASGRO fit values of $\Delta K_{th,LC}$, expressed in [MPa$\sqrt{m}$], for the tested stress ratios.

R	Experimental value	NASGRO fit
−2	7.17	7.24
-1	4.62 5.01	4.82
0	2.58	2.58
0.7	1.79 1.84	1.82

valleys in the net-shape surface, and sub-surface defects in the contour region for the samples subjected to Hirtisation®. In net-shape specimens, Figs. 7(a) and 7(b), crack initiation was predominantly linked to deep, sharp features. These features consisted of partially molten powder particles attached to fully molten material, leading to high stress concentration zones. Furthermore, fractographic analyses revealed defects in the contour regions, marked in purple.

In contrast, fractographies of samples subjected to Hirtisation® revealed three distinct types of crack initiation zones: (i) crack initiating at the bottom of deep valleys (Fig. 8(a)), similar to those observed in net-shape samples but with wavy character; (ii) defects connected to the surface affected by corrosion at the top, suggesting exposure during the Hirtisation® process, with the bottom

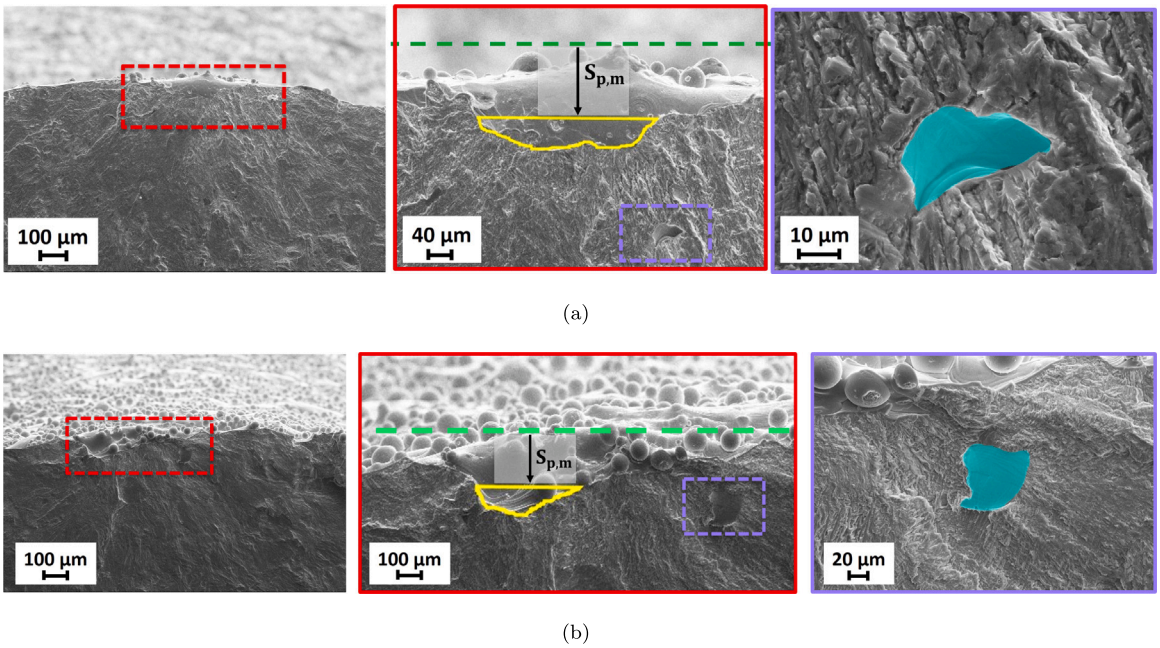

Fig. 7. Fractographies of net-shape specimens: (a) and (b) crack initiation from deep and sharp features typical of net-shape topography with detail on internal defect in contour region.

remaining unaffected, likely due to limited electrolyte penetration (Fig. 8(c)); and (iii) cracks originating from surface-adjacent defects without signs of internal corrosion (Fig. 8(b)).

For cracks initiated from troughs (type i), both in the net-shape condition and after Hirtisation®, considering the crack depth as the whole height of what is detectable on the fracture plane leads to an overestimation of the defect size. Based on the approach proposed by Barricelli et al. [52], a reference line was positioned using a surface roughness-based method to accurately calculate the defect size. The method includes the following steps:

- Identify the external features (i.e. un-molten particles attached to the surface which affect the roughness measurements but do not contribute the defect depth) in the fractography images;
- Starting from the highest feature, move downwards by a distance equal to the mean peak height value $S_{p,m}$ obtained from roughness measurements for the specific surface condition;
- Define the defect size at the fracture origin as the area of the region beneath the reference line.

The Murakami's parameter ($\sqrt{\text{area}}$) was then measured with a digital image analysis software [59]. The following rules were applied for determining the Murakami's parameter:

- Defect characterized with an aspect ratio (width over depth) 2c/a < 10, $\sqrt{\text{area}}$ was calculated as the square root of the measured area at the fracture origin;
- Defect characterized by an aspect ratio 2c/a ≥ 10, $\sqrt{\text{area}}$ was calculated as $\sqrt{10} \cdot t_{max}$, where t_{max} is the maximum depth measured from the reference line to the defect contour.

4.2. Failure mechanisms

Both micrographs and fracture surfaces of net-shape samples reveal defects located in the contour region of the material that were highlighted in purple on the fractographies, see for example Figs. 7(a) and 7(b). These defects can be attributed to voids generated at the neighbouring spots as well as the contouring-hatching interface [60]. Such defects did not lead to crack initiation and then failure when the specimens were in net-shape condition. The case of a fatigue specimen provides a notable exemplification of the phenomenon. The SEM imaging of its fracture surface, reported in Fig. 9(a), depicts multiple crack initiation points originating from a shallow net-shape feature; with micrography, on the other hand, it was possible to observe a typical contour anomaly located beneath the surface (see Fig. 9(b)) and from which a crack was nucleated, although it did not lead to the failure of the specimen. Sharper edges and, effectively, a larger size caused the net-shape feature to develop a stronger crack driving force with respect to the sub-surface feature, in spite of the larger effective dimension of this latter class of anomalies (as shown in Fig. 9(e)). For these reasons surface roughness, for non-treated condition, is more detrimental than sub-surface defects, in agreement with previous studies [12,61–66].

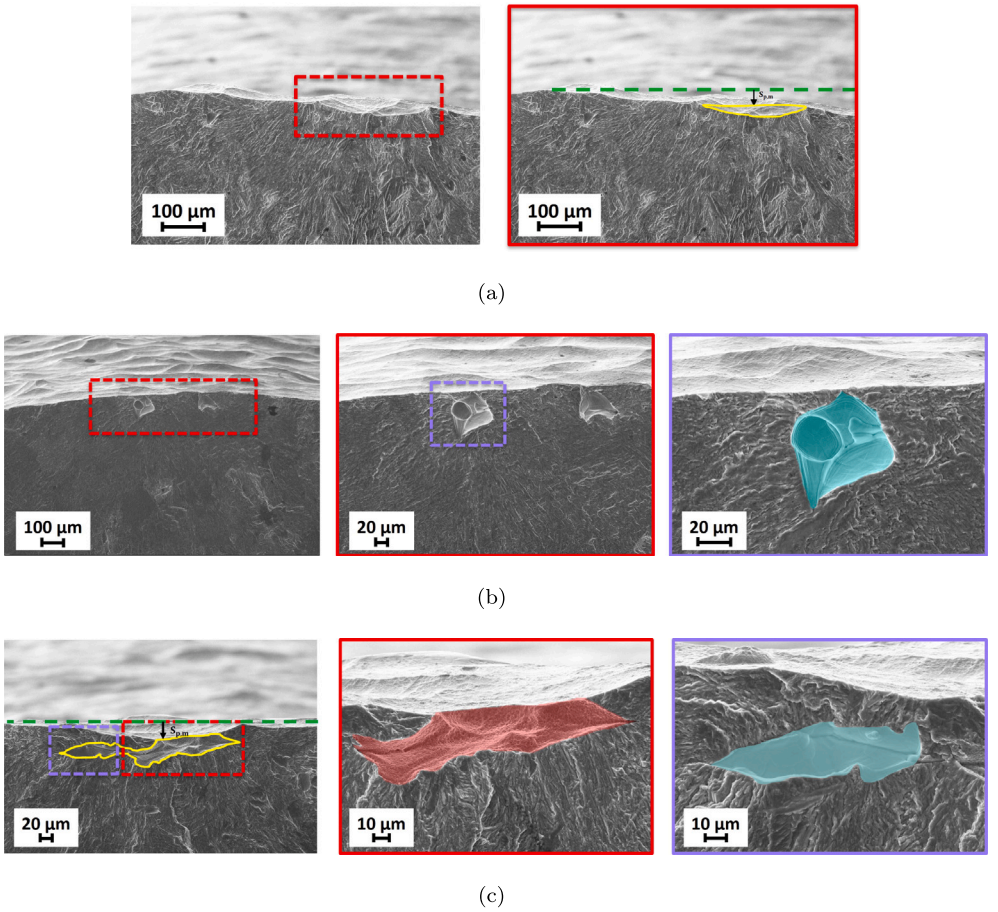

Fig. 8. Fractographies of specimens after Hirtisation®: (a) crack initiation from deep wavy valleys, (b) crack initiation from closed defects without sign of corrosion, (c) crack initiation from defect etched at the top (red region) with enclosed portions (light blue zone).

The reduction of the cross section in samples subjected to Hirtisation® is represented by the grey area between the net-shape surface and the contour region in Fig. 10. This process led to an improvement in surface roughness due to the removal of the deep and sharp valleys typical of net-shape surface condition, as it was highlighted in Section 3.2. However, the Hirtisation® treatment caused the largest contouring defects to become the anomalies at the origin of fracture, as seen from the fracture surfaces; these flaws, in fact, were either characterized by a shorter distance to the surface of the samples (as in Fig. 8(b)) or completely exposed to the open environment (as in Fig. 8(c)).

4.3. Statistical analysis of critical defects

Following the concepts of extreme value statistics (EVS) [67], the size of the most critical flaws observed from fracture surface imaging was fitted with a largest extreme value distribution (LEVD) [68]:

$$F_{\mathrm{LEVD}}(x) = \exp\left\{-\exp\left[\frac{-(x-\lambda)}{\delta}\right]\right\} \tag{3}$$

in which x is the defect size, while λ and δ are,respectively, the location and shape parameters of the distribution.

A summary of the LEVD parameters for both surface conditions is reported in Table 7, along with the 50% percentile defect size $\sqrt{\mathrm{area}}_{50\%}$ and the average aspect ratio $(\frac{a}{c})_{avg}$, calculated averaging the $(\frac{a}{c})$ values observed on the fracture surfaces. Fig. 11 displays the probability plots of the largest defects found on the fracture surfaces of net-shape and Hirtisation® specimens. The solid line represents the 50% regression line, while the dashed lines represent the 95% confidence band.

The Gumbel probability plots of the failure initiation defects detected on the samples subjected to Hirtisation® (Fig. 11(b)) distinguished the two types of critical defects: those originated from elongated valleys and those related to sub-surface features (i.e., contouring). The latter type of defects was found to be larger in size, confirming that the benefits introduced by the Hirtisation® process, such as the improvements in surface roughness, are partially offset by the presence of more critical contour defects. If crack

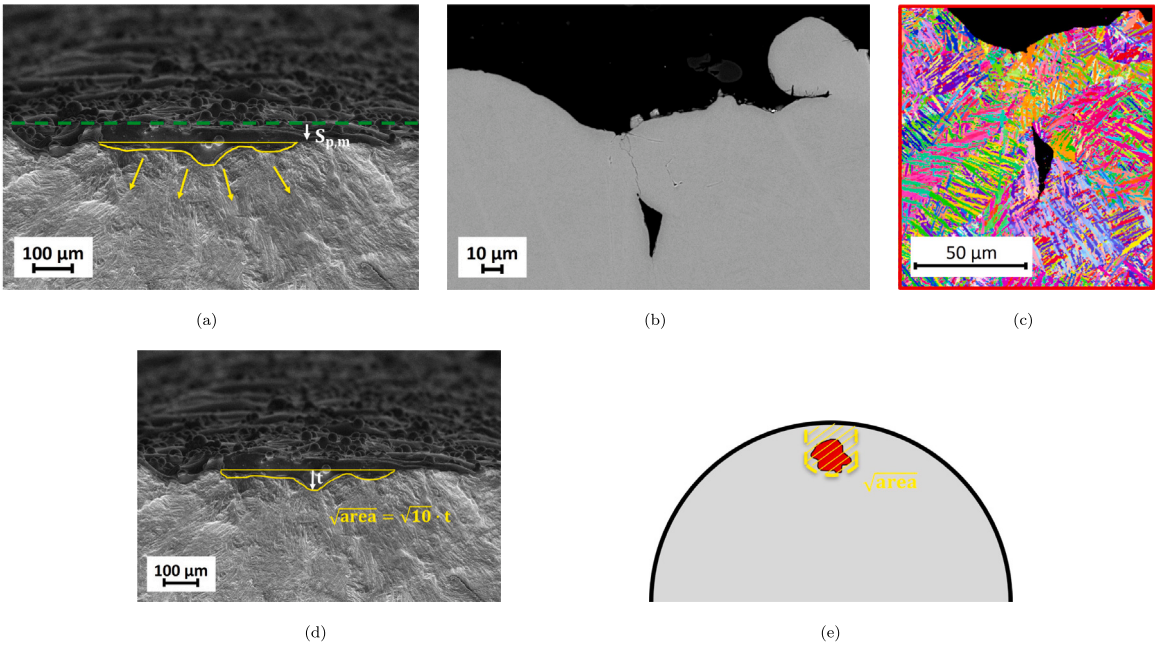

Fig. 9. A relevant example of failure mechanism in net-shape case: (a) fracture origin with positioning of the reference line; (b) defect in the contour region from which initiate crack without causing failure; (c) microstructure in the region around defect; (d) evaluation of the killer defects size from the fracture surface; (e) evaluation of the effective sub-surface defect size.

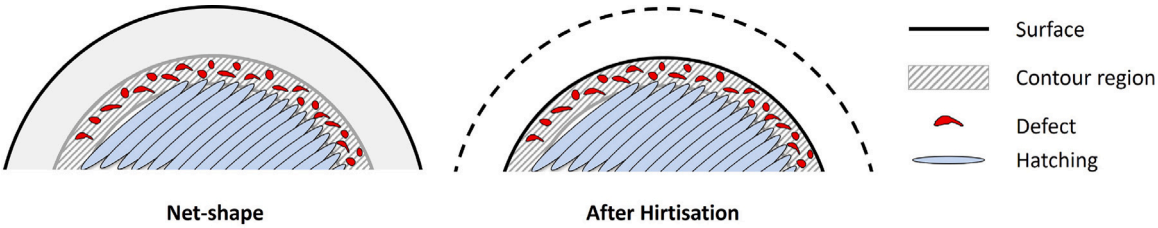

Fig. 10. Scheme of the cross section of axial specimens before and after Hirtisation® post-process: the surface features of net-shape condition were removed (dashed black line) and the defects located inside contour region (red features in dashed grey area) approaching the surface.

Table 7
Summary of LEVD parameters: comparison between net-shape surface and post-Hirtisation®.

Surface condition	λ [µm]	δ [µm]	$\sqrt{area}_{50\%}$ [µm]	$(a/c)_{avg}$
Net-shape	88	26	98	0.2
Post-Hirtisation®	66	16	72	1

initiation had been solely due to surface roughness features, the improvements in fatigue strength would have been more significant; this is further discussed in Section 5.2.

In the probability plot related to net-shape specimens, Fig. 11(a), no distinctions are highlighted since all killer defects are represented by sharp features typical of the surface topography.

5. Modelling of fatigue properties

5.1. Fatigue strength model

The Kitagawa–Takahashi diagram [69] describes the variation of the fatigue limit as a function of defect size. One of the most widely accepted models for this diagram is the equation proposed by El-Haddad [70], which is expressed with the Murakami's

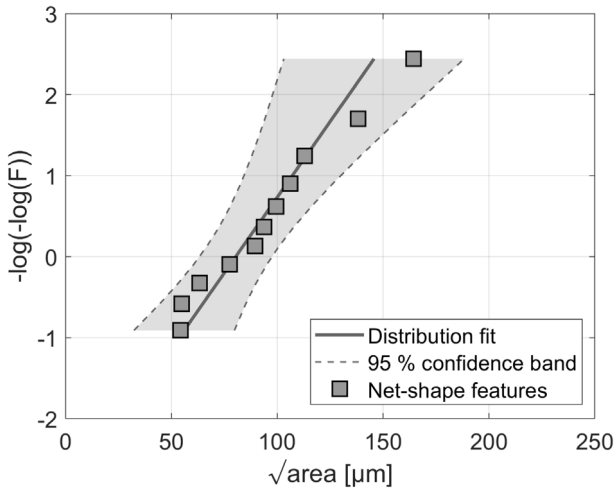

(a)

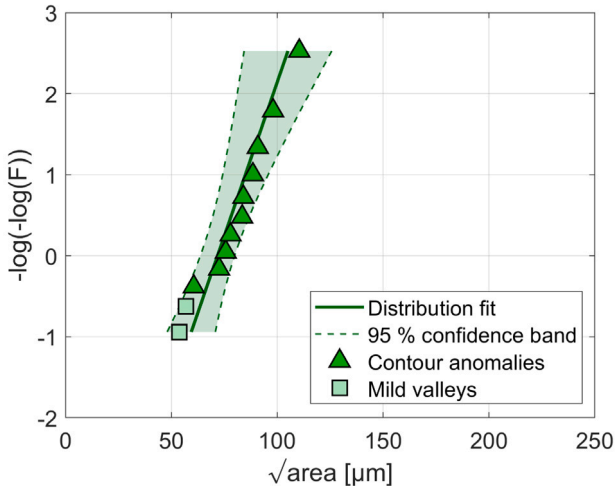

(b)

Fig. 11. LEVD probability plot of the largest defect found on fracture surfaces: (a) net-shape specimens, (b) post-Hirtisation specimens.

parameter as follows:

$$\Delta\sigma_w = \Delta\sigma_{w,0} \cdot \sqrt{\frac{\sqrt{\text{area}}_0}{\sqrt{\text{area}} + \sqrt{\text{area}}_0}} \tag{4}$$

$$\sqrt{\text{area}}_0 = \frac{1}{\pi} \cdot \left(\frac{\Delta K_{th,LC}}{Y \cdot \Delta\sigma_{w,0}}\right)^2 \tag{5}$$

$\Delta\sigma_w$ is the fatigue strength of defective component, while $\Delta\sigma_{w,0}$ is the theoretical fatigue strength for the defect-free component and thus it is computed as $\Delta\sigma_{w,0} = 2 \cdot 0.4 \cdot \text{UTS}$; $\Delta K_{th,LC}$ was obtained from the fit of the NASGRO equation, see Fig. 6 and Table 6. The shape factor was set as Y = 0.65, in accordance with the surface killer defects detected from fractographies.

Table 8 summarizes the parameters for the El-Haddad model of the Kitagawa–Takahashi diagram (4). Fig. 12 presents the Kitagawa–Takahashi diagrams for both net-shape specimens and those treated with Hirtisation®, alongside the experimental results.

The comparison between the fatigue strength model and test data shows a good correlation between the predicted fatigue strength and the experimental results: in details, it can be seen in Figs. 12(a) and 12(b) that the fatigue strength model accurately describes the non-propagation of defects for the run-out specimens . This supports the use of fracture mechanics-based assessments in predicting the fatigue properties of Ti6Al4V produced by AM.

Table 8
El-Haddad model parameters for the present PBF-LB/Ti6Al4V alloy.

R	$\Delta K_{th,LC}$ [MPa$\sqrt{m}$]	$\Delta\sigma_{w,0}$ [MPa]	$\sqrt{area}_0$ [μm]
−1	4.827	949.6	19.4

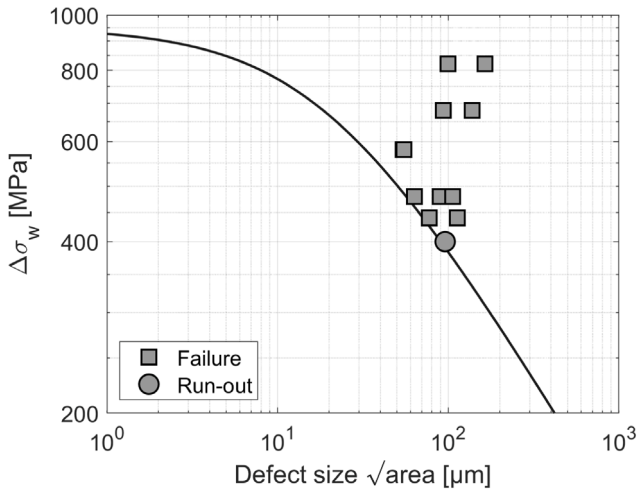

(a)

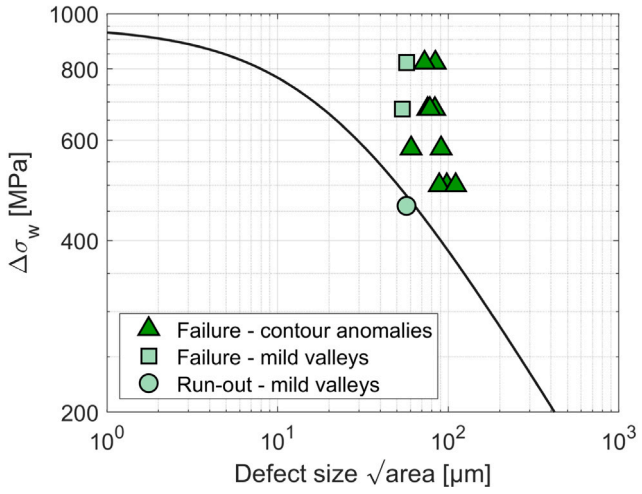

(b)

Fig. 12. Kitagawa diagrams for Ti6Al4V compared with experimental results on specimens: (a) Net-shape, (b) post-Hirtisation®.

Indeed, Fig. 12(b) also shows that failures due to defects generated by contouring are characterized by larger sizes compared to crack initiation from mild valleys in specimens treated with Hirtisation®.

5.2. Life predictions of specimens

Life predictions were conducted by considering the initial defect size and aspect ratio, based on the failure initiating defects observed on the fracture surfaces of the tested samples. Table 7 lists the initial crack sizes and aspect ratios used in the crack propagation algorithm for each series of samples, i.e., net-shape and after Hirtisation®.

The fatigue life estimates were carried out under the following assumptions:

- the crack growth model adopted was the NASGRO equation fitted as described in Fig. 6;

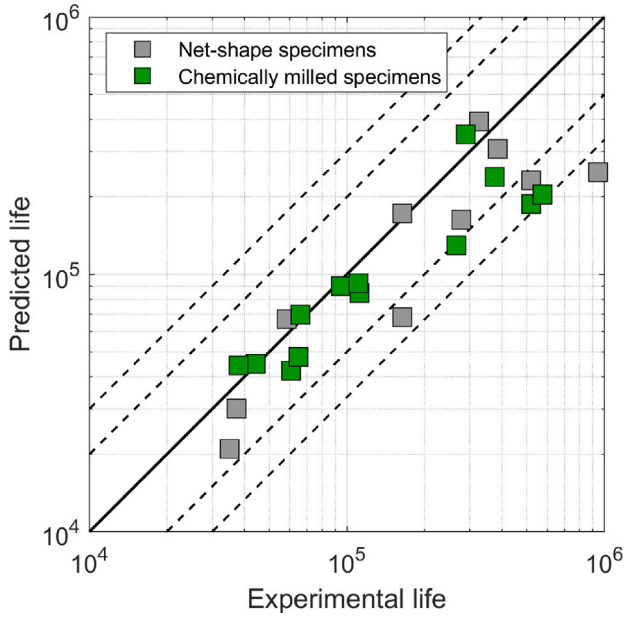

Fig. 13. Comparison between life predicted with propagation algorithm based on NASGRO equation and the experimental life for net-shape condition and after Hirtisation®.

- the stress intensity factor solution is the one proposed by Newman and Raju [71];
- the failure condition depends on the following:

1. for surface cracks: crack depth, a, equal to one third of specimen's thickness or crack width, c, equal to 0.4 the specimen's width;
2. for embedded cracks: crack depth, a, equal to a quarter of specimen's thickness or crack width, c, equal to a quarter of specimen's width;
3. maximum net-section stress higher than 90% of the flow stress, σ_{flow};
4. maximum stress intensity factor, K_{max}, higher than $0.7 \cdot K_{IC}$, where K_{IC} is the fracture toughness.

A comparison between the experimental data and predictions using the fatigue crack growth algorithm is presented in Fig. 13 for both surface conditions. The continuous black line represents the locus of agreement between the predictions and the experimental results, while the dashed lines indicate a factor 2 and 3 deviation between predictions and experiments. It can be observed that the majority of predictions are conservative, because in the analysis the nucleation of cracks from the defects is not considered. This effect is potentially more significant at the lowest stress levels.

This result can be seen also from the S–N diagrams reported in Figs. 14(a) and 14(b). The experimental S–N diagrams were generated by fitting the data points in the finite life region with an equation of the type $N_f = A \cdot \Delta\sigma^B$, together with the 95% failure probability regions marked with the dashed grey lines. These results confirm that the failure of PBF-LB/Ti6Al4V components can be well described with a fatigue crack growth model based on the NASGRO equation. However, further discussion is required for the case of life predictions for the post-Hirtisation® specimens. The failure of these specimens can be attributed to two types of defects: surface troughs or subsurface contouring defects. Fig. 14(b) presents life estimates for three different initial crack assumptions: (i) the continuous blue line represents life predictions for a crack size corresponding to the 50% percentile of the probability plot, considering all defect types observed on the fracture surfaces; (ii) the dotted blue line reflects predictions for a defect size equal to the mean value of wavy deep trough defects (see Fig. 11(b)); and (iii) the dashed blue line indicates life predictions for a defect size corresponding to the mean value of contour defects.

These life predictions suggest that, for specimens treated with Hirtisation®, fatigue performance in the fatigue limit region could be improved by approximately 35% in the case of failure driven by surface defects than the case of sub-surface contouring defects. However, the presence of contour defects, which are brought to the surface by the Hirtisation® process, reduces this potential benefit. The dimensions of these contour defects are comparable to those of surface defects found on the fracture surfaces of net-shape samples. As a final result, experiments show that the Hirtisation® process still yields a 14% increase in the fatigue limit ($\Delta\sigma_w$ = 480 MPa vs. $\Delta\sigma_w$ = 420 MPa), though this improvement is less pronounced than expected given the enhancement in surface quality. In perspective, this finding suggests that the adoption of the Hirtisation® process should be accompanied by careful selection of process parameters to avoid subsurface defects, even at the expense of surface quality, which can subsequently be improved by the process itself.

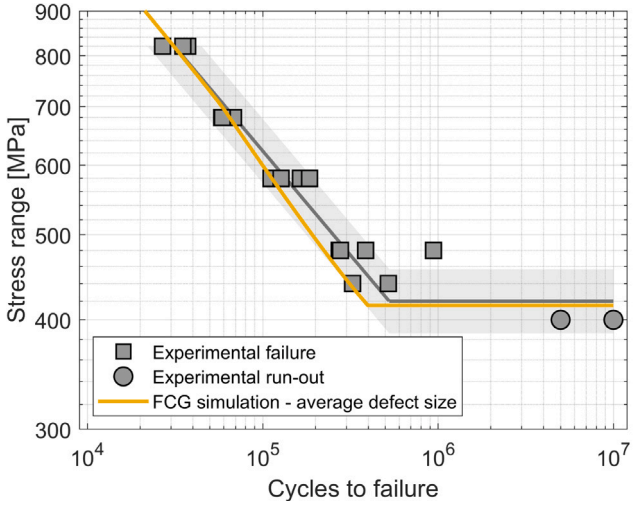

(a)

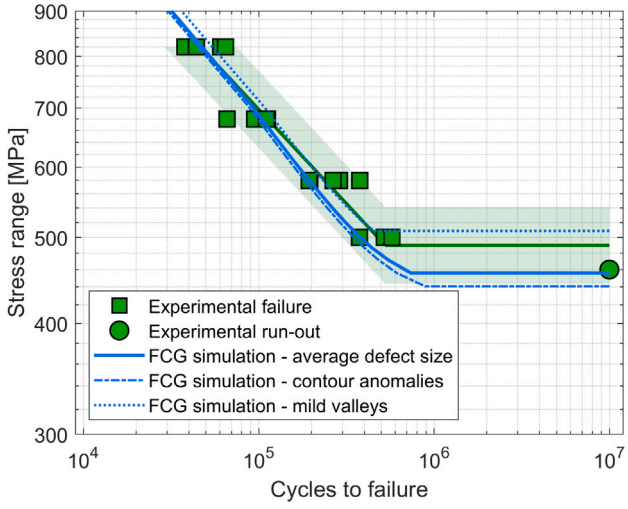

(b)

Fig. 14. Life predictions for specimens: (a) net-shape, (b) post-Hirtisation®.

6. Conclusions

This study analysed the impact of Hirtisation® post process on the surface quality and on the fatigue performances of PBF-LB/Ti6Al4V alloy. A wide experimental campaign on fatigue specimens was performed exploring two surface conditions: net-shape and after Hirtisation®. The main conclusions are here summarized:

- the Hirtisation® process significantly improves the roughness and surface quality for net-shape surface of Ti6Al4V;
- The analysis of fracture surfaces of the fatigue samples shows that failure is mainly driven by two types of defects: (i) deep and sharp valleys on the surface, (ii) sub-surface features in the contour region;
- In net-shape condition, surface roughness is more detrimental than sub-surface defects, even if in some cases short cracks were observed to originate from sub-surface defects without causing failure;
- After chemical milling by Hirtisation®, due to an insufficient material removal, sub-surface anomalies are brought closer to the surface and they become the critical features triggering fatigue failures;
- The benefits introduced by Hirtisation® are not completely exploited because of the harmful contour sub-surface defects near the surface; this led to a limited improvement of the fatigue limit, i.e. + 14%, when compared to the fatigue limit estimation with shallow valleys;

- The process parameters (either the PBF-LB or the chemical milling ones) should be carefully selected, to avoid that sub-surface anomalies could impair the potential fatigue strength enhancement due to improved surface quality.

CRediT authorship contribution statement

Tatiana Risposi: Writing – original draft, Visualization, Data curation. **Lorenzo Rusnati:** Writing – review & editing, Visualization, Data curation. **Luca Patriarca:** Writing – review & editing, Visualization, Methodology. **Alex Hardaker:** Methodology, Investigation. **Dawid Luczyniec:** Writing – review & editing, Resources. **Stefano Beretta:** Writing – review & editing, Supervision, Methodology, Funding acquisition, Conceptualization.

Declaration of competing interest

The authors declare the following financial interests/personal relationships which may be considered as potential competing interests: Stefano Beretta reports financial support was provided by European Space Agency. If there are other authors, they declare that they have no known competing financial interests or personal relationships that could have appeared to influence the work reported in this paper.

Acknowledgements

The study was conducted within the call-off order of the European Space Agency (ESA/ESTEC) ‘‘ESA Additive Manufacturing Benchmarking’’, contract number 4000133245/20/NL/AR/idb. The project involved ESA/ESTEC, The Manufacturing Technology Centre (MTC) and Politecnico di Milano (PoliMi).

Data availability

Data will be made available on request.

References

[1] H. Bikas, P. Stavropoulos, G. Chryssolouris, Additive manufacturing methods and modelling approaches: a critical review, Int. J. Adv. Manuf. Technol. 83 (2016) 389–405, http://dx.doi.org/10.1007/s00170-015-7576-2.
[2] E. Uhlmann, R. Kersting, T.B. Klein, M.F. Cruz, A.V. Borille, Additive manufacturing of titanium alloy for aircraft components, Procedia Cirp 35 (2015) 55–60, http://dx.doi.org/10.1016/j.procir.2015.08.061.
[3] P. Singh, H. Pungotra, N.S. Kalsi, On the characteristics of titanium alloys for the aircraft applications, Mater. Today: Proc. 4 (8) (2017) 8971–8982, http://dx.doi.org/10.1016/j.matpr.2017.07.249.
[4] A. Bandyopadhyay, F. Espana, V.K. Balla, S. Bose, Y. Ohgami, N.M. Davies, Influence of porosity on mechanical properties and in vivo response of Ti6Al4V implants, Acta Biomater. 6 (4) (2010) 1640–1648, http://dx.doi.org/10.1016/j.actbio.2009.11.011.
[5] B. Vrancken, L. Thijs, J.-P. Kruth, J. Van Humbeeck, Heat treatment of Ti6Al4V produced by selective laser melting: Microstructure and mechanical properties, J. Alloys Compd. 541 (2012) 177–185, http://dx.doi.org/10.1016/j.jallcom.2012.07.022.
[6] J. Sun, Y. Yang, D. Wang, Parametric optimization of selective laser melting for forming Ti6Al4V samples by Taguchi method, Opt. Laser Technol. 49 (2013) 118–124, http://dx.doi.org/10.1016/j.optlastec.2012.12.002.
[7] J.J. Lewandowski, M. Seifi, Metal additive manufacturing: a review of mechanical properties, Annu. Rev. Mater. Res. 46 (2016) 151–186, http://dx.doi.org/10.1146/annurev-matsci-070115-032024.
[8] S. Liu, Y.C. Shin, Additive manufacturing of Ti6Al4V alloy: A review, Mater. Des. 164 (2019) 107552, http://dx.doi.org/10.1016/j.matdes.2018.107552.
[9] W.E. Frazier, Metal additive manufacturing: a review, J. Mater. Eng. Perform. 23 (2014) 1917–1928, http://dx.doi.org/10.1007/s11665-014-0958-z.
[10] D. Herzog, V. Seyda, E. Wycisk, C. Emmelmann, Additive manufacturing of metals, Acta Mater. 117 (2016) 371–392, http://dx.doi.org/10.1016/j.actamat.2016.07.019.
[11] H.D. Nguyen, A. Pramanik, A. Basak, Y. Dong, C. Prakash, S. Debnath, S. Shankar, I. Jawahir, S. Dixit, D. Buddhi, A critical review on additive manufacturing of Ti-6Al-4V alloy: Microstructure and mechanical properties, J. Mater. Res. Technol. 18 (2022) 4641–4661, http://dx.doi.org/10.1016/j.jmrt.2022.04.055.
[12] E. Wycisk, A. Solbach, S. Siddique, D. Herzog, F. Walther, C. Emmelmann, Effects of defects in laser additive manufactured Ti-6Al-4V on fatigue properties, Phys. Procedia 56 (2014) 371–378, http://dx.doi.org/10.1016/j.phpro.2014.08.120.
[13] K.S. Chan, M. Koike, R.L. Mason, T. Okabe, Fatigue life of titanium alloys fabricated by additive layer manufacturing techniques for dental implants, Met. Mater. Trans. A 44 (2013) 1010–1022, http://dx.doi.org/10.1007/s11661-012-1470-4.
[14] T.M. Mower, M.J. Long, Mechanical behavior of additive manufactured, powder-bed laser-fused materials, Mater. Sci. Eng.: A 651 (2016) 198–213, http://dx.doi.org/10.1016/j.msea.2015.10.068.
[15] A. Triantaphyllou, C.L. Giusca, G.D. Macaulay, F. Roerig, M. Hoebel, R.K. Leach, B. Tomita, K.A. Milne, Surface texture measurement for additive manufacturing, Surf. Topogr.: Metrol. Prop. 3 (2) (2015) 024002, http://dx.doi.org/10.1088/2051-672X/3/2/024002.
[16] A. Townsend, N. Senin, L. Blunt, R. Leach, J. Taylor, Surface texture metrology for metal additive manufacturing: a review, Precis. Eng. 46 (2016) 34–47, http://dx.doi.org/10.1016/j.precisioneng.2016.06.001.
[17] M. Neikter, F. Forsberg, R. Pederson, M.-L. Antti, P. Åkerfeldt, S. Larsson, P. Jonsén, G. Puyoo, Defect characterization of electron beam melted Ti-6Al-4V and alloy 718 with X-ray microtomography, Aeronaut. Aerosp. Open Access J. 2 (3) (2018) 139–145, http://dx.doi.org/10.15406/aaoaj.2018.02.00044.
[18] J. Pegues, M. Roach, R.S. Williamson, N. Shamsaei, Surface roughness effects on the fatigue strength of additively manufactured Ti-6Al-4V, Int. J. Fatigue 116 (2018) 543–552, http://dx.doi.org/10.1016/j.ijfatigue.2018.07.013.
[19] J. Gockel, L. Sheridan, B. Koerper, B. Whip, The influence of additive manufacturing processing parameters on surface roughness and fatigue life, Int. J. Fatigue 124 (2019) 380–388, http://dx.doi.org/10.1016/j.ijfatigue.2019.03.025.
[20] S. Beretta, S. Romano, A comparison of fatigue strength sensitivity to defects for materials manufactured by AM or traditional processes, Int. J. Fatigue 94 (2017) 178–191, http://dx.doi.org/10.1016/j.ijfatigue.2016.06.020.

[21] N. Sanaei, A. Fatemi, Defects in additive manufactured metals and their effect on fatigue performance: A state-of-the-art review, Prog. Mater. Sci. 117 (2021) 100724, http://dx.doi.org/10.1016/j.pmatsci.2020.100724.
[22] A. Mostafaei, C. Zhao, Y. He, S.R. Ghiaasiaan, B. Shi, S. Shao, N. Shamsaei, Z. Wu, N. Kouraytem, T. Sun, et al., Defects and anomalies in powder bed fusion metal additive manufacturing, Curr. Opin. Solid State Mater. Sci. 26 (2) (2022) 100974, http://dx.doi.org/10.1016/j.cossms.2021.100974.
[23] H. Gong, K. Rafi, H. Gu, T. Starr, B. Stucker, Analysis of defect generation in Ti–6Al–4V parts made using powder bed fusion additive manufacturing processes, Addit. Manuf. 1 (2014) 87–98, http://dx.doi.org/10.1016/j.addma.2014.08.002.
[24] R. Cunningham, S.P. Narra, C. Montgomery, J. Beuth, A. Rollett, Synchrotron-based X-ray microtomography characterization of the effect of processing variables on porosity formation in laser power-bed additive manufacturing of Ti-6Al-4V, JOM 69 (2017) 479–484, http://dx.doi.org/10.1007/s11837-016-2234-1.
[25] Z. Chen, X. Wu, D. Tomus, C.H. Davies, Surface roughness of selective laser melted Ti-6Al-4V alloy components, Addit. Manuf. 21 (2018) 91–103, http://dx.doi.org/10.1016/j.addma.2018.02.009.
[26] Z. Chen, S. Cao, X. Wu, C.H. Davies, Surface roughness and fatigue properties of selective laser melted Ti–6Al–4V alloy, in: Additive Manufacturing for the Aerospace Industry, Elsevier, 2019, pp. 283–299, http://dx.doi.org/10.1016/B978-0-12-814062-8.00015-7.
[27] P. Karimi, C. Schnur, E. Sadeghi, J. Andersson, Contour design to improve topographical and microstructural characteristics of alloy 718 manufactured by electron beam-powder bed fusion technique, Addit. Manuf. 32 (2020) 101014, http://dx.doi.org/10.1016/j.addma.2019.101014.
[28] A. Kleen, E. Glaubitz, J. Gockel, Influence of Contour Offset in Laser Powder Bed Fusion on Melt Pool Behaviors, Surface Roughness and Sub-Surface Porosity, in: Proceedings Solid Freeform Pubblication Symposium, 2024, http://dx.doi.org/10.26153/tsw/58089.
[29] V. Sandell, P. Åkerfeldt, T. Hansson, M.-L. Antti, Fatigue fracture characterization of chemically post-processed electron beam powder bed fusion Ti–6Al–4V, Int. J. Fatigue 172 (2023) 107673, http://dx.doi.org/10.1016/j.ijfatigue.2023.107673.
[30] J. Berglund, J. Holmberg, K. Wärmefjord, R. Söderberg, Detailed evaluation of topographical effects of hirtisation post-processing on electron beam powder bed fusion (PBF-EB) manufactured Ti-6Al-4V component, Precis. Eng. 85 (2023) http://dx.doi.org/10.1016/j.precisioneng.2023.10.007.
[31] V. Sandell, J. Nilsson, T. Hansson, P. Åkerfeldt, M.-L. Antti, Effect of chemical post-processing on surfaces and sub-surface defects in electron beam melted Ti-6Al-4V, Mater. Charact. 193 (2022) 112281, http://dx.doi.org/10.1016/j.matchar.2022.112281.
[32] M. Kahlin, H. Ansell, D. Basu, A. Kerwin, L. Newton, B. Smith, J. Moverare, Improved fatigue strength of additively manufactured Ti6Al4V by surface post processing, Int. J. Fatigue 134 (2020) 105497, http://dx.doi.org/10.1016/j.ijfatigue.2020.105497.
[33] M. Basha, S. Basha, V. Jain, M. Sankar, State of the art on chemical and electrochemical based finishing processes for additive manufactured features, Addit. Manuf. 58 (2022) 103028, http://dx.doi.org/10.1016/j.addma.2022.103028.
[34] Y. Sun, S. Gulizia, C. Oh, D. Fraser, M. Leary, Y. Yang, M. Qian, The influence of as-built surface conditions on mechanical properties of Ti-6Al-4V additively manufactured by selective electron beam melting, JOM 68 (2016) 791–798, http://dx.doi.org/10.1007/s11837-015-1768-y.
[35] S. Bagehorn, T. Mertens, D. Greitemeier, L. Carton, A. Schoberth, Surface finishing of additive manufactured Ti-6Al-4V-a comparison of electrochemical and mechanical treatments, in: 6th Eur Conf Aerosp Sci, 2015.
[36] B. Wysocki, J. Idaszek, J. Buhagiar, K. Szlązak, T. Brynk, K.J. Kurzydłowski, W. Święszkowski, The influence of chemical polishing of titanium scaffolds on their mechanical strength and in-vitro cell response, Mater. Sci. Eng.: C 95 (2019) 428–439, http://dx.doi.org/10.1016/j.msec.2018.04.019.
[37] N. Stelzer, T. Sebald, M. Hatzenbichler, B. Bonvoisin, B. Lubos, M. Scheerer, Properties of surface engineered metallic parts prepared by additive manufacturing, 2021.
[38] E. Beevers, D. Neumayer, B. Bonvoisin, A. Brandão, S. Hansal, M. Doppler, T. Rohr, B. Van Hooreweder, Effect of hirtisation treatment on surface quality and mechanical properties of AlSi10Mg samples produced by laser powder bed fusion, Mater. Today Commun. 38 (2024) 108042, http://dx.doi.org/10.1016/j.mtcomm.2024.108042.
[39] N. Stelzer, M. Scheerer, Z. Simon, L. Bača, T. Sebald, H. Gschiel, M. Hatzenbichler, B. Bonvoisin, Mechanical properties of surface engineered metallic parts prepared by additive manufacturing, in: The European Conference on Spacecraft Structures, Materials and Environmental Testing, 2018.
[40] J. Gumpinger, A. Brandão, E. Beevers, T. Rohr, T. Ghidini, S. Beretta, S. Romano, Expression of additive manufacturing surface irregularities through a flaw-based assessment, in: Symposium on Structural Integrity of Additive Manufactured Parts, ASTM International, 2020, pp. 234–249, http://dx.doi.org/10.1520/STP162020180098.
[41] J. Berglund, J. Holmberg, K. Wärmefjord, R. Söderberg, Detailed evaluation of topographical effects of hirtisation post-processing on electron beam powder bed fusion (PBF-EB) manufactured Ti-6Al-4V component, Precis. Eng. 85 (2024) 319–327, http://dx.doi.org/10.1016/j.precisioneng.2023.10.007.
[42] ASTM E466-21, Standard practice for conducting force controlled constant amplitude axial fatigue tests of metallic Materials1, 2021, http://dx.doi.org/10.1520/E0466-21.
[43] ASTM F3637-23, Standard guide for additive manufacturing of metal - finished part properties - methods for relative density measurement, 2023.
[44] R. Pippan, The growth of short cracks under cyclic compression, Fatigue Fract. Eng. Mater. Struct. 9 (5) (1987) 319–328, http://dx.doi.org/10.1111/j.1460-2695.1987.tb00459.x.
[45] M.A. James, S.C. Forth, J.A. Newman, Load history effects resulting from compression precracking, J. ASTM Int. 2 (9) (2005) JAI12025.
[46] S. Cao, Y. Zou, C.V.S. Lim, X. Wu, Review of laser powder bed fusion (LPBF) fabricated Ti-6Al-4V: process, post-process treatment, microstructure, and property, Light: Adv. Manuf. 2 (3) (2021) 313–332, http://dx.doi.org/10.37188/lam.2021.020.
[47] M. Benedetti, E. Torresani, M. Leoni, V. Fontanari, M. Bandini, C. Pederzolli, C. Potrich, The effect of post-sintering treatments on the fatigue and biological behavior of Ti-6Al-4V ELI parts made by selective laser melting, J. Mech. Behav. Biomed. Mater. 71 (2017) 295–306, http://dx.doi.org/10.1016/j.jmbbm.2017.03.024.
[48] H. Galarraga, R.J. Warren, D.A. Lados, R.R. Dehoff, M.M. Kirka, P. Nandwana, Effects of heat treatments on microstructure and properties of Ti-6Al-4V ELI alloy fabricated by electron beam melting (EBM), Mater. Sci. Eng.: A 685 (2017) 417–428, http://dx.doi.org/10.1016/j.msea.2017.01.019.
[49] E.-. ASTM, Standard practice for statistical analysis of linear or linearized stress-life, american society for testing and materials, 2010.
[50] W. Dixon, The up-and-down method for small samples, J. Amer. Statist. Assoc. 60 (312) (1965) 967–978, http://dx.doi.org/10.1080/01621459.1965.10480843.
[51] S. Beretta, L. Patriarca, M. Gargourimotlagh, A. Hardaker, D. Brackett, M. Salimian, J. Gumpinger, T. Ghidini, A benchmark activity on the fatigue life assessment of AlSi10Mg components manufactured by L-PBF, Mater. Des. 218 (2022) 110713, http://dx.doi.org/10.1016/j.matdes.2022.110713.
[52] L. Barricelli, L. Patriarca, A. Du Plessis, S. Beretta, Orientation-dependent fatigue assessment of Ti6Al4V manufactured by L-PBF: Size of surface features and shielding effect, Int. J. Fatigue 168 (2023) 107401, http://dx.doi.org/10.1016/j.ijfatigue.2022.107401.
[53] L. Patriarca, A. D'Andrea, M. Cova, L. Rusnati, S. Beretta, Cyclic R-curve measurements for structural metallic alloys, Adv. Eng. Mater. 2400447, http://dx.doi.org/10.1002/adem.202400447.
[54] S. Leuders, M. Thöne, A. Riemer, T. Niendorf, T. Tröster, H.a. Richard, H. Maier, On the mechanical behaviour of titanium alloy TiAl6V4 manufactured by selective laser melting: Fatigue resistance and crack growth performance, Int. J. Fatigue 48 (2013) 300–307, http://dx.doi.org/10.1016/j.ijfatigue.2012.11.011.
[55] M.T. Hasib, H.E. Ostergaard, X. Li, J.J. Kruzic, Fatigue crack growth behavior of laser powder bed fusion additive manufactured Ti-6Al-4V: Roles of post heat treatment and build orientation, Int. J. Fatigue 142 (2021) 105955, http://dx.doi.org/10.1016/j.ijfatigue.2020.105955.
[56] S.W.R. Institute, NASGRO reference manual version 8.1, 2016.

[57] V. Cain, L. Thijs, J. Van Humbeeck, B. Van Hooreweder, R. Knutsen, Crack propagation and fracture toughness of Ti6Al4V alloy produced by selective laser melting, Addit. Manuf. 5 (2015) 68–76, http://dx.doi.org/10.1016/j.addma.2014.12.006.
[58] Y. Murakami, Metal Fatigue: Effects of Small Defects and Nonmetallic Inclusions, 2019.
[59] T. Ferreira, W. Rasband, Imagej user guide, ImageJ/ Fiji 1 (2012) 155–161.
[60] X. Zhao, S. Dadbakhsh, A. Rashid, Contouring strategies to improve the tensile properties and quality of EBM printed inconel 625 parts, J. Manuf. Process. 62 (2021) 418–429, http://dx.doi.org/10.1016/j.jmapro.2020.12.007.
[61] H. Masuo, Y. Tanaka, S. Morokoshi, H. Yagura, T. Uchida, Y. Yamamoto, Y. Murakami, Effects of defects, surface roughness and HIP on fatigue strength of Ti-6Al-4V manufactured by additive manufacturing, Procedia Struct. Integr. 7 (2017) 19–26, http://dx.doi.org/10.1016/j.prostr.2017.11.055.
[62] S. Moon, R. Ma, R. Attardo, C. Tomonto, M. Nordin, P. Wheelock, M. Glavicic, M. Layman, R. Billo, T. Luo, Impact of surface and pore characteristics on fatigue life of laser powder bed fusion Ti–6Al–4V alloy described by neural network models, Sci. Rep. 11 (1) (2021) 20424, http://dx.doi.org/10.1038/s41598-021-99959-6.
[63] R. Molaei, A. Fatemi, N. Phan, Significance of hot isostatic pressing (HIP) on multiaxial deformation and fatigue behaviors of additive manufactured Ti-6Al-4V including build orientation and surface roughness effects, Int. J. Fatigue 117 (2018) 352–370, http://dx.doi.org/10.1016/j.ijfatigue.2018.07.035.
[64] Y. Sun, S. Lu, S. Gulizia, C. Oh, D. Fraser, M. Leary, M. Qian, Fatigue performance of additively manufactured Ti-6Al-4V: surface condition vs. internal defects, JOM 72 (2020) 1022–1030, http://dx.doi.org/10.1007/s11837-020-04025-7.
[65] G. Kasperovich, J. Hausmann, Improvement of fatigue resistance and ductility of TiAl6V4 processed by selective laser melting, J. Mater. Process. Technol. 220 (2015) 202–214, http://dx.doi.org/10.1016/j.jmatprotec.2015.01.025.
[66] D. Greitemeier, F. Palm, F. Syassen, T. Melz, Fatigue performance of additive manufactured TiAl6V4 using electron and laser beam melting, Int. J. Fatigue 94 (2017) 211–217, http://dx.doi.org/10.1016/j.ijfatigue.2016.05.001.
[67] S. Beretta, Y. Murakami, Statistical analysis of defects for fatigue strength prediction and quality control of materials, Fatigue Fract. Eng. Mater. Struct. 21 (9) (1998) 1049–1065, http://dx.doi.org/10.1046/j.1460-2695.1998.00104.x.
[68] E. Gumbel, Statistics of Extremes, Courier Corporation, 2012.
[69] H. Kitagawa, Applicability of fracture mechanics to very small cracks or the cracks in the early stage, in: Proc. 2nd Int. Conf. on Mechanical Behaviour of Materials, 1976, pp. 627–631.
[70] Y. Murakami, Inclusion rating by statistics of extreme values and its application to fatigue strength prediction and quality control of materials, J. Res.-Natl. Inst. Stand. Technol. 99 (1994) http://dx.doi.org/10.6028/jres.099.032, 345–345.
[71] J. Newman Jr., I. Raju, Analysis of Surface Cracks in Finite Plates Under Tension or Bending Loads, Tech. Rep., 1979.